nature climate change

LETTERS

https://doi.org/10.1038/s41558-019-0637-z

Amplified Rossby waves enhance risk of concurrent heatwaves in major breadbasket regions

Kai Kornhuber[1,2,3*], Dim Coumou[4,5], Elisabeth Vogel[6], Corey Lesk[7], Jonathan F. Donges[5,8], Jascha Lehmann[5] and Radley M. Horton[7]

In an interconnected world, simultaneous extreme weather events in distant regions could potentially impose high-end risks for societies[1,2]. In the mid-latitudes, circumglobal Rossby waves are associated with a strongly meandering jet stream and might cause simultaneous heatwaves and floods across the northern hemisphere[3–6]. For example, in the summer of 2018, several heat and rainfall extremes occurred near-simultaneously[7]. Here we show that Rossby waves with wavenumbers 5 and 7 have a preferred phase position and constitute recurrent atmospheric circulation patterns in summer. Those patterns can induce simultaneous heat extremes in specific regions: Central North America, Eastern Europe and Eastern Asia for wave 5, and Western Central North America, Western Europe and Western Asia for wave 7. The probability of simultaneous heat extremes in these regions increases by a factor of up to 20 for the most severe heat events when either of these two waves dominate the circulation. Two or more weeks per summer spent in the wave-5 or wave-7 regime are associated with 4% reductions in crop production when averaged across the affected regions, with regional decreases of up to 11%. As these regions are important for global food production, the identified teleconnections have the potential to fuel multiple harvest failures, posing risks to global food security[8].

Extreme weather events have a devastating impact on society and are expected to occur more frequently in a warming climate due to anthropogenic greenhouse gas emissions[9,10]. The societal impacts of extreme weather events can be amplified when extremes occur near-simultaneously in time[1,2], as economic chains are increasingly interlinked and world markets make production failures in one location felt in others[11]. Day-to-day weather variability in the mid-latitudes is predominantly controlled by the dynamics of the jet stream and its interaction with cyclones and anticyclones, leading to co-variability of weather in far-away regions[12,13]. This effect is strongest when the circulation features weakened west to east flow and large north–south meanders develop in the jet[5,14]. Indeed, statistical analyses have shown that, during periods of such amplified Rossby waves, cold and warm extremes occur more frequently across the hemisphere[6,15]. However, the exact regions, severity and possible co-occurrence of heat extremes have not yet been quantified systematically. Here, we show that simultaneous extreme events in specific northern hemisphere (NH) regions may not happen by chance but because they are linked via two modes of recurrent Rossby wave patterns with wavenumbers 5 and 7 (waves 5 and 7 hereon). These waves exhibit preferred phase positions while others do not[7,16,17]. We first quantify the importance of those Rossby waves for heat events in single regions. Next, we employ event coincidence analysis[18] to assess how the probability of heat extremes occurring simultaneously in several regions relate to the occurrence of the identified Rossby wave patterns. We then assess the impact of wave-5 and wave-7 events within a summer on annual crop production of countries within the identified regions, employing the composite approach introduced by Lesk and others[19].

The stationary disturbances of mid-latitudinal flow brought by large-scale mountain ridges and land–ocean boundaries have an effect on the preferred phases of Rossby waves[16,20] (for simplicity, 'waves' hereon). To quantify this phase-locking behaviour in the NH mid-latitudes, we create probability density distributions of the phase position of synoptic scale waves (waves 5–8) during weeks when their amplitude is high and compare these to the distribution of all remaining weeks (Fig. 1). Wave amplitudes and phases were assessed by applying a Fourier analysis on weekly means of the meridionally averaged meridional wind, following Kornhuber and others[7] (see Methods for details). The wave phase is defined with respect to the dateline (180°) as a reference longitude (see Figs. 3a and 4a, later, for an idealized depiction of a wave in its preferred phase position). We find that waves 5 and 7 exhibit a higher tendency to 'phase locking', as their phase distributions show a symmetric single peak. This single peak in the probability distribution implies that the associated ridges and troughs reoccur over the same regions: their phases are 'locked'. In contrast, waves 6 and 8 exhibit broad asymmetric distributions, so their tendency to reoccur within a confined longitudinal range is much less pronounced (Fig. 1 and Supplementary Fig. 1).

As a consequence of a more confined phase distribution, composite fields of meridional winds of weeks characterized by an amplified wave 5 or 7 (Fig. 2a,c) show a clear circumglobal wave pattern. In contrast, composites of waves 6 and 8 show only regionally significant patterns but no hemispheric extent (Supplementary Fig. 2). This is because most (>50%) high-amplitude waves 5 and 7 have phase positions within a window smaller than a quarter of their wavelength ($\frac{1}{2}\ \pi$, Fig. 1), but waves 6 and 8 do not. Composite fields of near-surface air temperature (SAT) anomalies and upper

[1]Earth Institute, Columbia University, New York, NY, USA. [2]Atmospheric, Oceanic and Planetary Physics, University of Oxford, Oxford, UK. [3]National Centre for Atmospheric Science, Leeds, UK. [4]Institute for Environmental Studies, VU University Amsterdam, Amsterdam, the Netherlands. [5]Earth System Analysis, Potsdam Institute for Climate Impact Research, Member of the Leibniz Association, Potsdam, Germany. [6]Australian-German Climate & Energy College, The University of Melbourne, Melbourne, Victoria, Australia. [7]Columbia University, Lamont Doherty Earth Observatory, Palisades, NY, USA. [8]Stockholm Resilience Centre, Stockholm University, Stockholm, Sweden. *e-mail: kk3397@columbia.edu

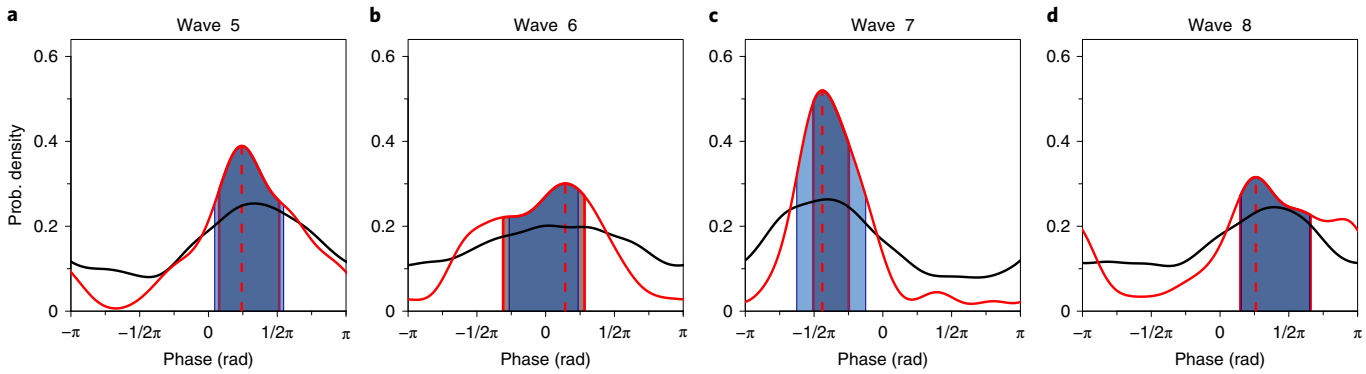

Fig. 1 | Phase locking of Rossby waves. a–d, Probability densities of the phase positions of waves 5 (**a**), 6 (**b**), 7 (**c**) and 8 (**d**) during June–August based on weekly averaged meridional wind fields. Probability densities of weeks with high wave amplitudes (>1.5σ, red solid line, $N = 45, 47, 44, 46$) are compared to all remaining weeks (black solid line). Regions within the 25th and 75th percentiles around the mean position are marked with red vertical lines. The range $\pm\pi/4$ around the mean is shown in light blue. The maximum is marked with a red dashed line. A strong symmetric single-peak distribution is found for wave 5 and wave 7 during weeks with high amplitudes, while wave 6 and wave 8 exhibit a broad asymmetric distribution (Supplementary Fig. 1).

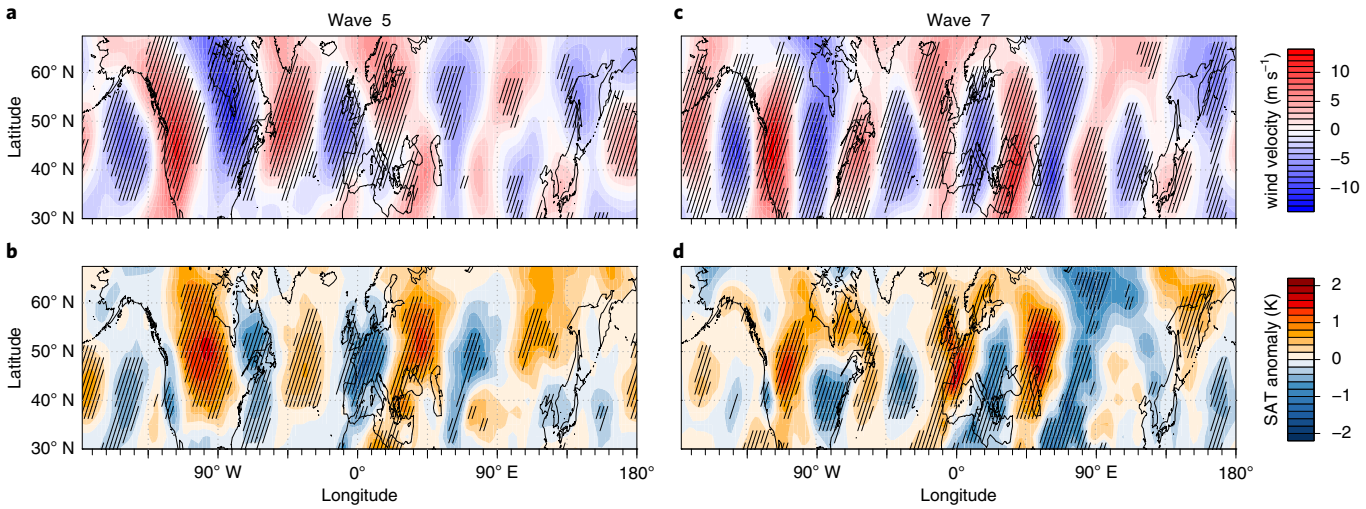

Fig. 2 | Circumglobal teleconnections and associated surface weather in summer. a–d, Composite plots of meridional wind velocity (**a**,**c**) and surface temperature anomalies (**b**,**d**) during weeks of high-amplitude waves 5 and 7. Statistically significant deviations from climatology are hatched ($P \leq 0.05$).

troposphere meridional winds (300 mbar) are shifted by about a quarter of a wavelength, with positive temperature anomalies found between northward (positive) and southward (negative) meridional winds depicting circumglobal patterns of alternating warm and cold anomalies (Fig. 2b,d). This alignment of wind fields and surface temperature indicates that the wave patterns are generally barotropic in nature, especially over the western hemisphere[14].

The circumglobal nature of the identified Rossby wave patterns comprises recurrent teleconnections that link heat events in far-away regions across the mid-latitudes[7,21]. To quantify their importance for heat extremes of different magnitudes, we define regions of interest by clustering neighbouring grid points over land where SATs are significantly different from their seasonal climatology (that is, the hatched regions over land in Fig. 2b,d). Only regions with a size larger than 10 grid points within the mid-latitudinal belt (35° N to 65° N) are included, resulting in three regions for each wave. For wave 5, these are Central North America (1: CNA), Eastern Europe (2: EEU) and East Asia (3: EAS) (Fig. 3a), and for wave 7 Western/Central North America (1: WCNA), Western Europe (2: WEU) and Western Asia (3: WAS) (Fig. 4a and Supplementary Figs. 4 and 5). We used event coincidence analysis[18] (ECA) to quantify the co-occurrence of heat events and high-amplitude wave-5 and wave-7 events, A_w, with $w \in 5, 7$. ECA is a statistical method that allows quantification of the simultaneity of events contained in two series of observations, with statistical significance assessed by random shuffling. We define event time-series of heat extremes $h_{s,T}$ in each region using weekly averages of detrended temperature anomalies based on two parameters that reflect their intensity and spatial coverage, respectively: (1) a grid point-based temperature threshold T in units of standard deviations σ above the climatological mean and (2) the ratio s of grid points in a specific region i with temperature exceeding T. High-amplitude wave events are determined on a weekly basis by selecting those weeks during which the wave amplitude exceeds the 1.5σ threshold above the mean (for details see Supplementary Methods). We computed the coincidence rates of weekly heat events $h_{s,T}$ coinciding with weeks of high-amplitude wave A_w amplitude as ECA($h_{s,T}$,A_w). Event coincidence rates (coincidence rates, hereon) can range between zero and one, where zero means that none of the events coincide and one means that all events coincide.

We find that the probability of stronger and more widespread heat events increases in the presence of amplified waves specifically

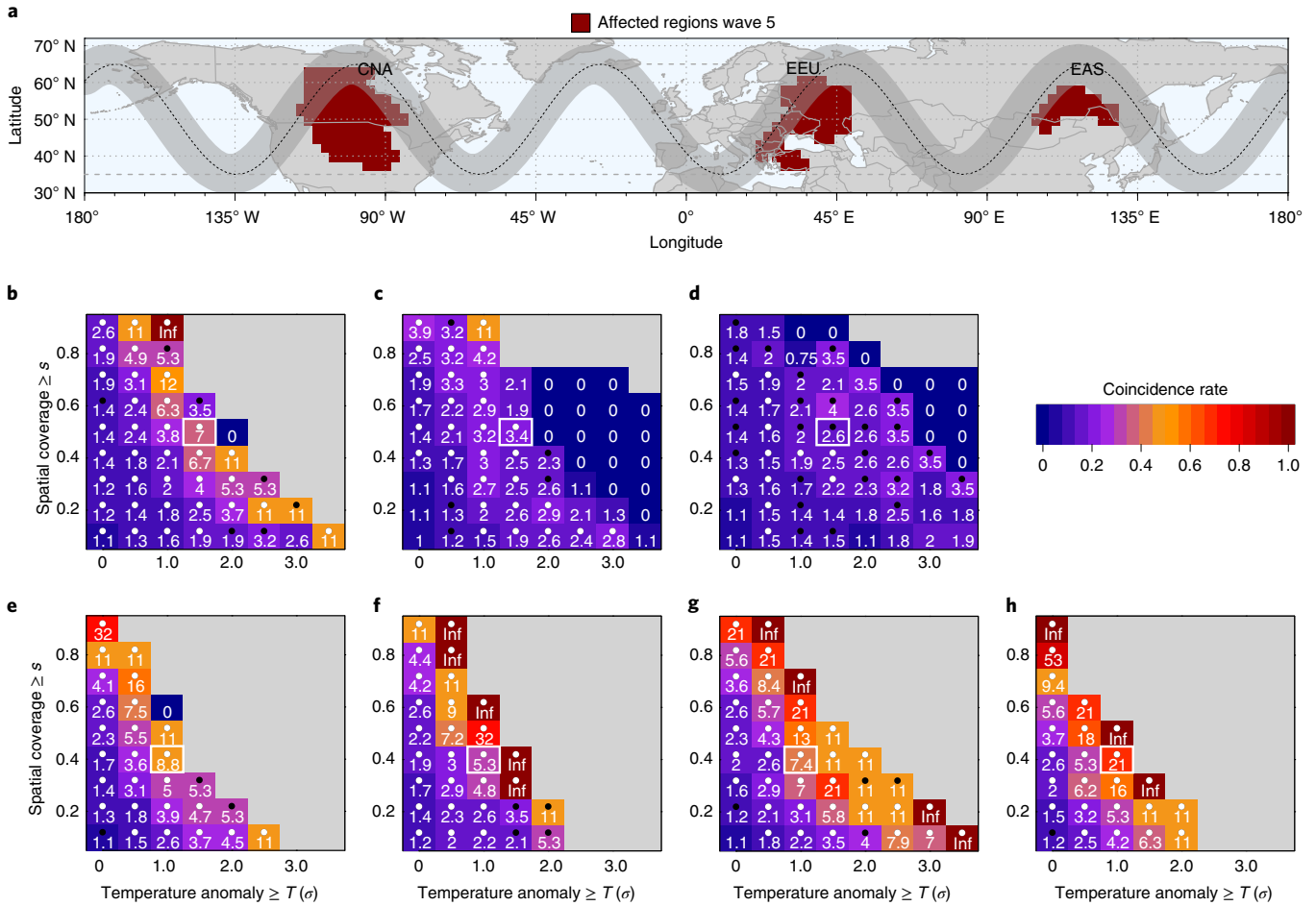

Fig. 3 | Coincidence of heatwaves in regions teleconnected by wave 5. a, Regions affected by anomalous heat during wave-5 events and an idealized depiction of the circulation when wave 5 is in its preferred phase with the width and position of the maximum (black dotted line) reflecting values shown in Fig. 1a. **b**–**d**, Regional coincidence rates of amplified wave-5 conditions with heat events of different intensity and spatial extent for CNA (**b**), EEU (**c**) and EAS (**d**). The most severe heat events can be found in the upper right corner of each plot. The numbers refer to the factor by which wave events amplify the respective heat events. This factor is given as 'Inf' when all observed heat events coincide with wave events relative to non-event weeks. Statistical significance of the coincidence rates at the 99% (95%) confidence level is marked with a white (black) dot. Examples discussed in the text are highlighted by a white box. **e**–**g**, As in **b**–**d** but for simultaneous heat events in two regions: CNA and EEU (**e**); CNA and EAS (**f**); EEU and EAS (**g**). **h**, Coincidence rates based on all three identified regions.

for heat events co-occurring in more than one region (Figs. 3 and 4). Coincidence rates of wave-5 events and heat events in each of the three regions are presented as a heatmap in Fig. 3b–d. Each tile corresponds to heat events of a specific severity, with temperature anomaly T on the horizontal axis (in units of standard deviation above the mean) and spatial extent S on the vertical axis (as area fraction relative to the respective region). The number in the tile corresponds to the factor by which the heat event's probability changes during wave events (see Supplementary Figs. 10 and 11 for the total number of events). For example, in CNA, we find ten heat events with $T > 1.5$ and $S > 0.5$ ($h_{s>0.5,\,T>1.5}$) in total, four of which coincide with an amplified wave 5 (white box, Fig. 3b). Thus, the coincidence rate is $\mathrm{ECA}\left(h_{s>0.5,\,T>1.5}, A_{w5}\right) = 0.4$. As there are 45 wave-5 weeks detected within the total of 520 June–August (JJA) weeks (1979–2018), that leaves 475 non-wave-5 weeks. Thus, the probability of an $h_{s>0.5,\,T>1.5}$ heat event occurring during a wave-5 event week ($P = \frac{4}{45} \approx 0.09$) is seven times higher than a normal week in summer ($P = \frac{6}{475} \approx 0.01$) (white box, Fig. 3b). For EEU, this probability is 3.4 times higher, while for EAS it is 2.6 times higher (white boxes, Fig. 3c,d). The most extreme event detected for EEU relates to the Russian heatwave of 2010 ($h_{s>0.8,\,T>3}$).

To quantify the importance of waves 5 and 7 for heat events occurring simultaneously in multiple regions, time-series were generated for heat events $h_{s,T}$ occurring in two (three) regions simultaneously (see Supplementary Figs. 12 and 13 for an alternative approach, which shows the same qualitative results). To exemplify, we use $h_{s>0.4,\,T>1}$ events (white box, Fig. 3e–h), and 11 simultaneous events are found for CNA and EEU. The probability of such coinciding heat events during a high-amplitude wave 5 is 8.8 times higher than during all remaining weeks (white box, Fig. 3e), while the probabilities for such events in CNA/EAS and EEU/EAS pairings are amplified by factors of 5 and 7, respectively, during wave-5 events (white boxes, Fig. 3f,g). When analysing coincidence of $h_{s>0.4,\,T>1}$ events across all three regions, we find that their occurrence probability during wave-5 events increases by a factor of 21 compared to all remaining weeks (Fig. 3h).

Proceeding with the regional analysis for wave 7, we find that WEU is most affected, with all four of the most severe heat events ($h_{s>0.7,\,T>2.5}$) coinciding with an amplified wave 7 (white outlined box, Fig. 4c; see Supplementary Fig. 11 for the total numbers of events). Two of the four events are from the summer of 2003. For regions WCNA and WAS, the highest significant coincidence

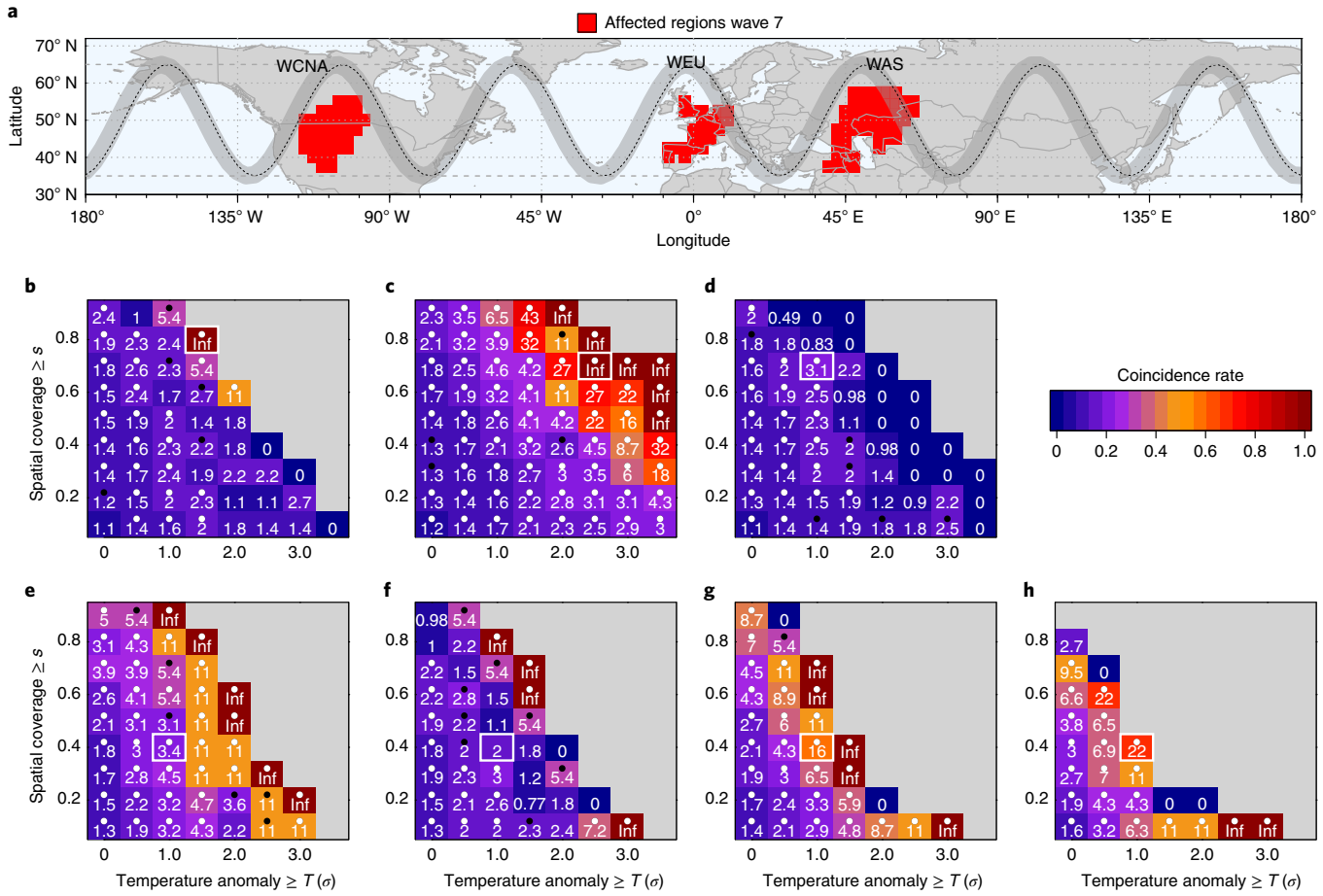

Fig. 4 | Coincidences of heatwaves in regions teleconnected by wave 7. a, Regions affected by anomalous heat during wave-7 events and an idealized depiction of the circulation when wave 7 is in its preferred phase with the width and position of the maximum (black dotted line) reflecting values shown in Fig. 1a. **b**–**d**, Regional coincidence rates of amplified wave-7 conditions with heat events of different intensity and spatial extent for WCNA (**b**), WEU (**c**) and WAS (**d**). The most severe heat events can be found in the upper right corner of each plot. The numbers refer to the factor by which wave events amplify the respective heat events. This factor is given as 'Inf' when all observed heat events coincide with wave events relative to non-event weeks. Statistical significance of coincidence rates at the 99% (95%) confidence level is marked with a white (black) dot. Examples discussed in the text are highlighted by a white box. **e**–**g**, As in **b**–**d** but for simultaneous heat events in two regions: WCNA and WEU (**e**); WCNA and WAS (**f**); WEU and WAS (**g**). **h**, Coincidence rates based on all three identified regions.

rates are found for ($h_{s>0.8,T>1.5}$) and ($h_{s>0.7,T>1}$), in line with the overall signal of highest coincidence rates occurring for widespread events of high magnitude (white boxes, Fig. 4b,d). To exemplify coinciding heat events in multiple regions for wave 7, we again use $h_{s>0.4,T>1}$ events (white box, Fig. 4e–h), and find a threefold increase in probabilities for simultaneous events in WCNA and WEU. Detected events include the summers of 2003, 1983 and 2015. The factor in WCNA and WAS is 2 (but is not significant) and for WEU and WAS, we find a 16-fold increase in probability. The likelihood of the simultaneous occurrence of such an event in all three regions WCNA, WEU and WAS is 22 times higher during a wave-7 event compared to the remaining summer weeks, although only three events are identified in total, of which two coincide with a wave-7 event (Supplementary Fig. 11). Those include weeks in the extreme summers of 1983 and 2003 (see Supplementary Information for additional robustness tests related to wave amplitudes, phase positions and coincident heat events in the identified regions). We also find that waves 6 and 8 do have relevance for regional weather extremes, but as their phase-locking behaviour is less pronounced (Fig. 1b,d), fewer statements can be made about the locations in which they occur and, by extension, their physical linkages to simultaneous heat extremes in multiple regions (Supplementary Figs. 1, 2 and 16).

Some studies have reported an increase in waves 5 and 7 over recent summers[7,22]. Whether such trends are associated with anthropogenic climate change[23] or multidecadal variability requires further research. The wave event time-series used in this study do not show significant trends in event frequency over the period 1979–2018 (Supplementary Fig. 8). Nevertheless, even without changes in high-amplitude wave events, the intensity of heat events associated with those waves would be amplified due to increasing mean temperatures. Thus, the impacts of such events will probably become more severe, for example for the agricultural sector[24]. The regions affected by waves 5 and 7 account for a large fraction of global food production (Fig. 5): for wheat, the United States, France and Russia produce 42% and for maize the United States and France alone produce 57%[25,26]. The two wave patterns show a large overlap in North America, which might suggest added vulnerability to agricultural impacts. Simultaneous heatwaves and associated production declines in the region highlighted here might even have the potential to trigger shocks in global food supply as affected countries might impose export bans to ensure national food security[8].

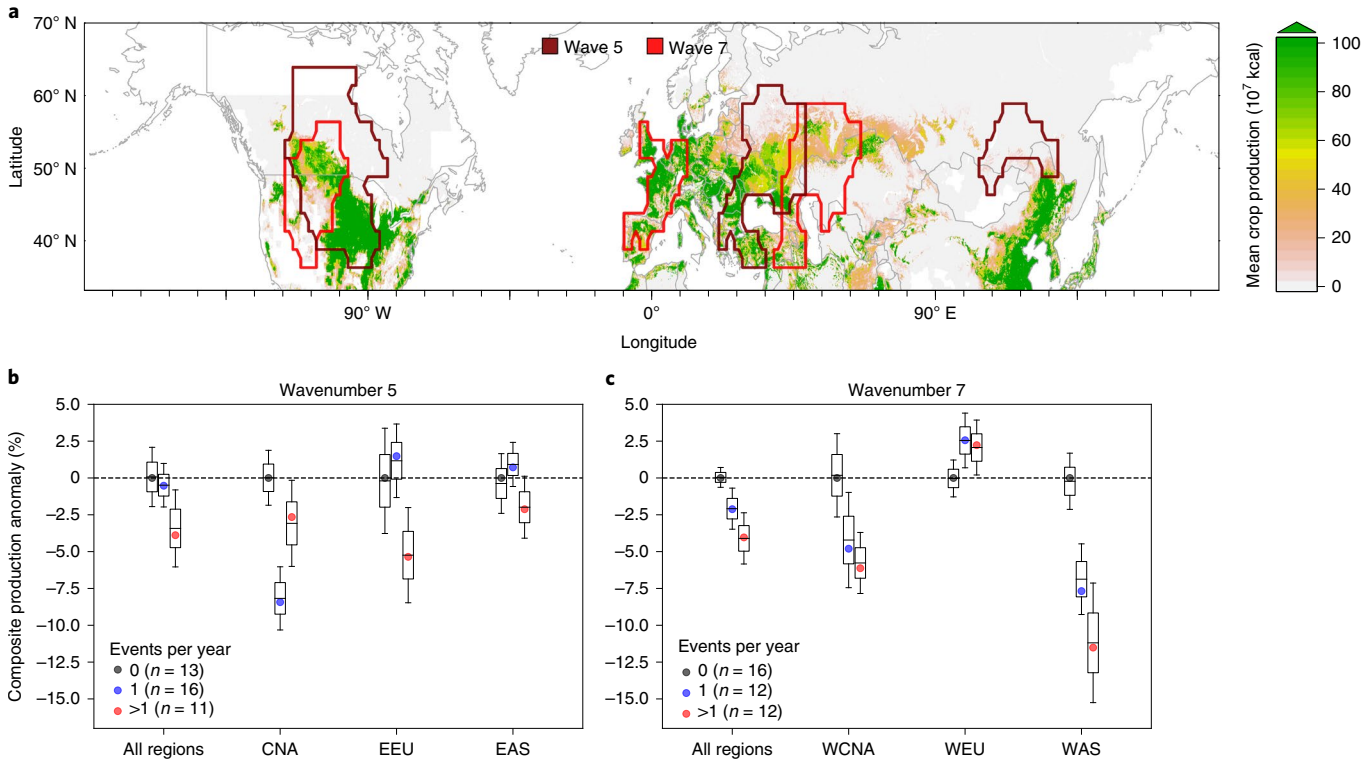

Fig. 5 | Crop production and teleconnected regions. a, Average crop production (2003–2007) for the major commodity crops maize, wheat, soybean and rice, converted to kcal (based on data from ref. [25]). Outlines of the regions affected by wave 5 and wave 7 are indicated in brown and red, respectively. Affected regions include the major breadbaskets in Central North America, Western and Eastern Europe. **b**, Annual composite production anomalies in affected regions based on the number of wave-5 events during JJA, shown as points: $n=0$ (grey), $n=1$ (blue) and $n>1$ (red) wave-5 events during JJA. Uncertainty ranges are shown as boxplots where boxes depict the 25th and 75th percentiles and whiskers indicate the lower and upper quartiles ±1.5 times the interquartile range of the composite uncertainty determined using a bootstrapping approach (see Supplementary section 'Uncertainty estimates'). Production anomalies are shown relative to the composite signal in years without a wave event. **c**, As in **b** but for wave-7 events. Wave events are found to negatively affect crop production in the identified regions, with WEU wave 7 as an exception.

The phase-locking behaviours of waves 5 and 7 pose enhanced risks, as heat events tend to occur repeatedly over the same regions. Using the composite method by Lesk and others[19] (see Methods for details), we find that the average crop production of all regions combined is indeed negatively affected by wave events, with a decrease of 4% in summers that feature more than one wave-5 or wave-7 event (Fig. 5b,c) relative to years with no wave events. This anomaly is significant for wave 7 at a 90% confidence level ($P=0.06$, Supplementary Table 1). Regionally, the effects are mostly negative, while for WEU a slight positive (but non-significant) effect is found on average. Crop production shortfalls at 95% confidence level are detected for CNA (wave 5) and WAS (wave 7) (Supplementary Table 1). Furthermore, years in which we identify simultaneous heat and wave events include years that saw spikes in food prices (2003, 2006 and 2012)[27]. Although, for 2003, we find a negative anomaly in crop production for WEU only (−7%), negative anomalies in several regions were observed for 2006 (WCNA, −9%; WEU, −4%; WAS, −8%) and 2012 (CNA, −9%; EEU, −16%). Although, food prices are affected by a number of factors[8,27] (for example, storage dynamics, management, accumulated effects of extreme events that occurred in previous years), those harvest losses probably contributed to the rise in crop prices in those years. Our study thus highlights the risks of the identified wave patterns on global and regional crop yield variability in the current climate. Further research is needed to quantify those risks under future climate projections and to assess the underlying drivers behind the recurrence and seasonality of the discussed Rossby wave patterns.

Online content

Any methods, additional references, Nature Research reporting summaries, source data, extended data, supplementary information, acknowledgements, peer review information; details of author contributions and competing interests; and statements of data and code availability are available at https://doi.org/10.1038/s41558-019-0637-z.

Received: 6 March 2019; Accepted: 23 October 2019;
Published online: 09 December 2019

References

1. Sarhadi, A., Ausín, M. C., Wiper, M. P., Touma, D. & Diffenbaugh, N. S. Multidimensional risk in a nonstationary climate: joint probability of increasingly severe warm and dry conditions. *Sci. Adv.* **4**, eaau3487 (2018).
2. Zscheischler, J. & Seneviratne, S. I. Dependence of drivers affects risks associated with compound events. *Sci. Adv.* **3**, e1700263 (2017).
3. Teng, H., Branstator, G., Wang, H., Meehl, G. A. & Washington, W. M. Probability of US heat waves affected by a subseasonal planetary wave pattern. *Nat. Geosci.* **6**, 1056–1061 (2013).
4. Schubert, S. D., Wang, H., Koster, R. D., Suarez, M. J. & Groisman, P. Y. Northern Eurasian heat waves and droughts. *J. Clim.* **27**, 3169–3207 (2014).
5. Kornhuber, K., Petoukhov, V., Petri, S., Rahmstorf, S. & Coumou, D. Evidence for wave resonance as a key mechanism for generating high-amplitude quasi-stationary waves in boreal summer. *Clim. Dynam.* **49**, 1961–1979 (2017).
6. Coumou, D., Petoukhov, V., Rahmstorf, S., Petri, S. & Schellnhuber, H. J. Quasi-resonant circulation regimes and hemispheric synchronization of extreme weather in boreal summer. *Proc. Natl Acad. Sci. USA* **111**, 12331–12336 (2014).

7. Kornhuber, K. et al. Extreme weather events in early summer 2018 connected by a recurrent hemispheric wave-7 pattern. *Environ. Res. Lett.* **14**, 054002 (2019).
8. Puma, M. J., Bose, S., Chon, S. Y. & Cook, B. I. Assessing the evolving fragility of the global food system. *Environ. Res. Lett.* **10**, 024007 (2015).
9. Schär, C. et al. The role of increasing temperature variability in European summer heatwaves. *Nature* **427**, 3926–3928 (2004).
10. Lehmann, J., Coumou, D. & Frieler, K. Increased record-breaking precipitation events under global warming. *Climatic Change* **132**, 501–515 (2015).
11. Levermann, A. Make supply chains climate-smart. *Nature* **506**, 27–29 (2013).
12. Branstator, G. Circumglobal teleconnections, the jet stream waveguide and the North Atlantic oscillation. *J. Clim.* **15**, 1893–1910 (2002).
13. Lau, K.-M. & Weng, H. Recurrent teleconnection patterns linking summertime precipitation variability over East Asia and North America. *J. Meteorol. Soc. Jpn* **80**, 1309–1324 (2002).
14. Petoukhov, V., Rahmstorf, S., Petri, S. & Schellnhuber, H. J. Quasiresonant amplification of planetary waves and recent northern hemisphere weather extremes. *Proc. Natl Acad. Sci. USA* **110**, 5336–5341 (2013).
15. Screen, J. A. & Simmonds, I. Amplified mid-latitude planetary waves favour particular regional weather extremes. *Nat. Clim. Change* **4**, 704–709 (2014).
16. Kornhuber, K. et al. Summertime planetary wave-resonance in the northern and southern hemisphere. *J. Clim.* **30**, 6133–6150 (2017).
17. Ding, Q. & Wang, B. Circumglobal teleconnection in the northern hemisphere summer. *J. Clim.* **18**, 3483–3505 (2005).
18. Donges, J., Schleussner, C. F., Siegmund, J. F. & Donner, R. V. Event coincidence analysis for quantifying statistical interrelationships between event time series. *Eur. Phys. J. Spec. Top.* **225**, 471–487 (2016).
19. Lesk, C., Rowhani, P. & Ramankutty, N. Influence of extreme weather disasters on global crop production. *Nature* **529**, 84–87 (2016).
20. White, R. H., Battisti, D. S. & Roe, G. H. Mongolian mountains matter most: impacts of the latitude and height of Asian orography on Pacific wintertime atmospheric circulation. *J. Clim.* **30**, 4065–4082 (2017).
21. Petoukhov, V. et al. The role of quasi-resonant planetary wave dynamics in recent boreal spring-to-autumn extreme events. *Proc. Natl Acad. Sci. USA* **113**, 6862–6867 (2016).
22. Lee, M. H., Lee, S., Song, H. J. & Ho, C. H. The recent increase in the occurrence of a boreal summer teleconnection and its relationship with temperature extremes. *J. Clim.* **30**, 7493–7504 (2017).
23. Mann, M. E. et al. Projected changes in persistent extreme summer weather events: the role of quasi-resonant amplification. *Sci. Adv.* **4**, eaat3272 (2018).
24. Schauberger, B. et al. Consistent negative response of US crops to high temperatures in observations and crop models. *Nat. Commun.* **8**, 13931 (2017).
25. Ray, D. K., Ramankutty, N., Mueller, N. D., West, P. C. & Foley, J. A. Recent patterns of crop yield growth and stagnation. *Nat. Commun.* **3**, 1293–1297 (2012).
26. Bren d'Amour, C., Wenz, L., Kalkuhl, M., Christoph Steckel, J. & Creutzig, F. Teleconnected food supply shocks. *Environ. Res. Lett.* **11**, 035007 (2016).
27. Schewe, J., Otto, C. & Frieler, K. The role of storage dynamics in annual wheat prices. *Environ. Res. Lett.* **12**, 054005 (2017).

Methods

Data. Meridional wind fields (300 mbar) and near-SAT fields were obtained from the NCEP/NCAR reanalysis[28]. These are provided on a 2.5 × 2.5 grid, limited to the satellite-based period (1979–2018). The results are robust against the choice of reanalysis dataset and chosen period (not shown).

Five-year average commodity crop yield data (t ha^{-1}) and harvested area fraction for maize, rice, wheat and soybean for 2003–2007 are based on data from ref. [25] (retrieved from http://www.earthstat.org/) on a 5 min × 5 min grid.

Nutrition data for maize, rice, wheat and soybean used for generating the results shown in Fig. 5 was taken from the United States Department of Agriculture, Agricultural Research Service (USDA) database (https://fdc.nal.usda.gov; maize, ndbNumber 20014; rice, ndbNumber 20040; wheat, ndbNumber 20076; soybean, ndbNumber 16108).

National annual yield data for Fig. 5 are based on the 'cereal, total' dataset from the Food and Agriculture Organization of the United Nations (FAO, freely available online at http://www.fao.org/faostat/en/#home). This dataset includes the 16 most important global cereal crops, including maize, wheat, rice and barley. For further information on this dataset see http://www.fao.org/es/faodef/fdef01e.htm.

Coincidence of heat events in identified regions, conditioned by wave events. An alternative approach to the one presented in Figs. 3 and 4 is to compare coincidence rates of heatwaves under the condition of high (normal) wave amplitude A_w ($\neg A_w$), for example ECA$\left(h_{s,T}|A_w, h_{s,T}|A_w\right)$ versus ECA$\left(h_{s,T}|\neg A_w, h_{s,T}|\neg A_w\right)$. Thus, in contrast to the analysis presented in Figs. 3 and 4, coincidence is not assessed between (co-occurring) heat events and wave events but between two heat events. This is done twice, first for those heat events that also fall together with a wave event, that is, the time-series are conditioned on heat events (Supplementary Fig. 12a–c for wave 5 and Supplementary Fig. 13a–c for wave 7). For this case we chose the following notation: ECA$\left(h_{s,T}|A_w, h_{s,T}|A_w\right)$. Second, coincidence analysis is performed for all remaining weeks as well (that is, conditioned on non-events, which we write as ECA$\left(h_{s,T}|\neg A_w, h_{s,T}|\neg A_w\right)$) shown in Supplementary Fig. 12d–f for wave 5 and Supplementary Fig. 13d–f for wave 7. When comparing coincidence rates between both, we find that heat events tend to co-occur more often when wave events are present, specifically for heat events that are widespread and of high temperature.

Analysis of waves 6 and 8. Waves 6 and 8 do carry relevance for regional weather extremes, but as they do not exhibit a preferred phase (for example, no particular phase locking, see Fig. 1), fewer statements can be made about the locations in which they occur (Supplementary Figs. 1, 2 and 16).

Wave amplitudes and phase positions. Wave amplitudes and phases were determined by applying fast Fourier transformation on the weekly averaged mid-latitudinal mean (37.5° N to 57.5° N) meridional wind velocities at the 300 mb level. A Fourier transformation decomposes the meridional wind into its basic components provided by sine functions: $\Psi = A\ \sin(kx - \varphi)$, dependent on amplitude A, wavenumber k, longitude x and phase φ. Although wavenumber k refers to the number of ridges and troughs a Rossby wave would exhibit around the globe, the amplitude A provides a notion of how dominant a respective wavenumber is. Phase φ describes the shift with respect to a reference longitude, which in our case is given by the 180° dateline. In our analysis we focus on wavenumbers 5–8 as the associated wavelengths are of synoptic scale and thus relevant for large-scale mid-latitude weather patterns.

Wave events. Wave events are defined by a 1.5σ threshold determined based on 520 weekly values in JJA (13 weeks a year) for the 1979–2018 period. For waves 5–8 we detect $N = 45, 47, 44, 46$ events, respectively. For a time-series of wave-5 and wave-7 events see Supplementary Fig. 8.

Temperature anomalies. Near-SAT anomalies were determined by subtracting the linear trend per grid point and day of year, thereby removing the climatological seasonal cycle and temperature trend before calculating weekly means.

Defining affected regions. Regions were defined by clusters of adjacent grid points (on a 2.5° × 2.5° grid) on land area showing statistically significant ($P < 0.05$) temperature anomalies during wave events (Fig. 3a for wave 5 and Fig. 4a for wave 7). Three regions were identified for each wavenumber. For wave 5 these are CNA (93 grid points), EEU (57 grid points) and EAS (24 grid points) and for wave 7 WCNA (40 grid points), WEU (24 grid points) and WAS (54 grid points). To further motivate the choice of regions, we generated one-point surface temperature coincidence maps with the central grid point x of each of the six regions. We used a local temperature threshold $T = 1\sigma$ to generate the event time-series for each given grid point and calculate coincidence statistics with the central grid point x (see Supplementary Fig. 3 for a map of NH σ values in JJA). During normal weeks with respect to waves 5 and 7, the grid points with the highest coincidence rates were localized around the central grid point x (Supplementary Fig. 4). During weeks of high-amplitude waves 5 and 7, a wave-like pattern emerges across the mid-latitudes (Supplementary Fig. 5). Areas with the highest coincidence rates are in good agreement with the regions selected for each wave, respectively (Figs. 3a and 4a). When calculating coincidence maps for a grid point far away from an identified region, the wave patterns are absent (not shown).

ECA. ECA was performed using the CoinCalc R package from ref. [29] following the methodology introduced in ref. [18]. The statistical significance of coincidence rates was tested using a Monte Carlo approach based on random shuffling of events in time ($N = 1{,}000$), employing a confidence level of 99% and 95%, respectively. ECA is conceptually related to simple Bayes approaches, but allows for a refined analysis by the possibility of accounting for different time window sizes for counting coincidences, time delays or conditional coincidences.

Aggregating crop production anomalies. We employed superposed epoch analysis (SEA), also known as compositing, following the methodology outlined in ref. [19]. SEA was introduced as a statistical method to isolate the signal of particular events in noisy time-series data. Here, we use SEA to test the influence of wave events on annual national crop production, aggregated across the countries that fall in the affected regions, as well as a hemispheric aggregation including all countries with affected regions, globally. We estimated the composite production anomaly for wave-event years by averaging standardized crop production anomalies across all years during which a wave event occurred and over all countries within a regional group. Crop production anomalies for a given country and event year were calculated as the deviation from a seven-year window mean centred around the event year, omitting the event itself from the mean, and dividing the resulting anomaly by this mean. For example, assuming 2000 is a year with a wave event, the production anomaly for this year and a given country is calculated as the production of 2000 minus the mean production of 1997–1999 and 2001–2003, divided by the mean production of the same six years. This approach provides standardized production anomalies (in %) for all countries and wave-event years. To accommodate the standardization procedure, the first and last three years of wave event time series are omitted. We estimated the composite by averaging crop production anomalies across the regional aggregations, and we presented the anomalies as relative to years in which no wave events occurred, by subtracting the average production anomaly in zero-event years from the signal in years with one (or more) wave event.

Uncertainty estimates of production anomalies. The uncertainty in the composite estimate was determined by repeating the SEA procedure on the production data using randomly sampled zero-event years as well as years with one (or more) wave event, generating 100 sets of composites for zero-event years as well as event years. Each bootstrap was based on a random subsample (without replacement) of the observed zero-event years as well as years with one (or more) wave event, and had a sample size of 0.9 of the original number of years; that is, 10% of years were left out in each bootstrapped sample. Based on the resampled control composites, the uncertainty around the composite production anomaly was computed across all regions as well as for each region separately. This was done for each wave, respectively.

Statistical significance of production anomalies. In addition to estimating the uncertainty bounds, we performed a statistical significance analysis of the crop production anomalies during wave events using bootstrapping. For each bootstrap sample, we reshuffled the wave events across the years so the overall number of 0-, 1- and >1-event years was equal to the observations, but the years were randomly distributed. Using SEA, we calculated the composite production anomalies for 0-, 1- and >1-event years in this random sample. We subsequently calculated the difference in composite production anomalies for 1-event minus 0-event years as well as >1-event minus 0-event years, as we did for the observations (globally and for regions). By repeating these steps ($N = 500$), we obtained an empirical distribution of the differences in production anomalies between zero-event and wave-event years. We then compared the magnitude of the observed difference in production (relative to zero-event years) to this empirical distribution by determining its percentile. If the production anomaly (relative to zero-event years) was smaller than the 5th (or 10th) percentile of the production anomalies in the empirical distribution, we considered it significantly negative (that is, we applied a one-sided statistical test to determine the significance of negative anomalies).

Assessed regions. National crop production datasets were grouped according to identified regions.

For wave 5: CNA (Canada, United States), EEU (Greece, Bulgaria, Moldova, North Macedonia, Ukraine, Romania, Serbia, Albania) and EAS (Mongolia, Russia, China). For wave 6: NA (Canada) and Central Europe (Albania, Greece, Poland, Lithuania, Croatia, Slovakia, Romania, Serbia, Bulgaria, North Macedonia, Kosovo). For wave 7: WCNA (Canada, United States), WEU (France, Switzerland, Spain, Portugal, United Kingdom, Belgium, Netherlands, Germany) and WAS (Turkey, Iran, Iraq, Armenia, Azerbaijan, Georgia, Russia, Kazakhstan). For wave 8: WEU (Spain, France, Belgium) and WAS (Russia, Turkey, Mongolia).

Data availability

The data used in this study can be obtained via the NCEP-NCAR website (https://www.esrl.noaa.gov/psd/data/gridded/data.ncep.reanalysis.html) and the FAOSTAT database of the United Nations Food and Agriculture Organization (http://www.fao.org/faostat/en/#data/QC).

Code availability

The codes used are available on request.

References

28. Kalnay et al. The NCEP/NCAR 40-year reanalysis project. *Bull. Am. Meteorol. Soc.* **77**, 437–470 (1996).
29. Siegmund, N. CoinCalc—a new R package for quantifying simultaneities of event series. *Comput. Geosci.* **98**, 64–72 (2017).

Acknowledgements

We thank the federal state of Brandenburg for the use of high-performance computing resources. This work was supported by the UK Natural Environment Research Council (NERC) National Centre for Atmospheric Science (NCAS) and NERC grant nos NE/P006779/1 and NE/N018001/1 (K.K.), the German Federal Ministry of Education and Research (BMBF; J.L. and D.C.), the Netherlands Organisation for Scientific Research (NWO; D.C.), the Leibniz Association project DominoES (J.F.D.) and the European Research Council Advanced Grant project ERA (J.F.D.).

Author contributions

K.K. conceived, designed and wrote the paper. K.K., E.V. and C.L. analysed the data. J.F.D., J.L., C.L., E.V., R.M.H. and D.C. helped with the design of the paper and co-wrote the manuscript.

Competing interests

The authors declare no competing interests.

Additional information

Supplementary information is available for this paper at https://doi.org/10.1038/s41558-019-0637-z.

Correspondence and requests for materials should be addressed to K.K.

Peer review information *Nature Climate Change* thanks Justin Mankin, Rachel White and the other, anonymous, reviewer(s) for their contribution to the peer review of this work.

Reprints and permissions information is available at www.nature.com/reprints.